ACS APPLIED MATERIALS & INTERFACES

www.acsami.org Research Article

Ultrasound-Triggered Assembly of Covalent Triazine Framework for Synthesizing Heteroatom-Doped Carbon Nanoflowers Boosting Metal-Free Bifunctional Electrocatalysis

Yong Zheng, Shan Chen, Kai A. I. Zhang,* Jixin Zhu, Jingsan Xu, Chao Zhang,* and Tianxi Liu

Cite This: *ACS Appl. Mater. Interfaces* 2021, 13, 13328−13337 Read Online

ABSTRACT: The construction of multiple heteroatom-doped porous carbon with unique nanoarchitectures and abundant heteroatom active sites is promising for reversible oxygen-involving electrocatalysis. However, most of the synthetic methods required the use of templates to construct precisely designed nanostructured carbon. Herein, we introduced an ultrasound-triggered route for the synthesis of a piperazine-containing covalent triazine framework (P-CTF). The ultrasonic energy triggered both the polycondensation of monomers and the assembly into a nanoflower-shaped morphology without utilizing any templates. Subsequent carbonization of P-CTF led to the formation of nitrogen, phosphorus, and fluorine tri-doped porous carbon (NPF@CNFs) with a well-maintained nanoflower morphology. The resultant NPF@CNFs showed high electrocatalytic activity and stability toward bifunctional electrolysis, which was better than the commercial Pt/C and IrO_2 electrocatalysts toward oxygen reduction reaction (ORR) and oxygen evolution reaction (OER), respectively. As a further demonstration, employing NPF@CNFs as air electrode materials resulted in an excellent performance of liquid-state and solid-state Zn-air batteries, showing great potentials of the obtained multiple heteroatom-doped porous carbon electrocatalysts for wearable electronics.

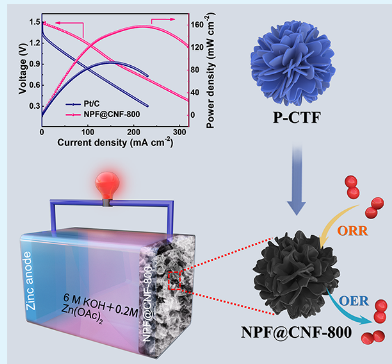

KEYWORDS: *carbon nanoflowers, ultrasound synthesis, covalent triazine framework, bifunctional electrocatalysis, Zn-air battery*

1. INTRODUCTION

Rechargeable zinc−air (Zn-air) batteries have gained considerable research and industrial attention owing to their low cost, high energy density, environmental friendliness, and so on.[1] In particular, flexible solid-state Zn-air batteries featuring safety, flexibility, and convenience are favorable candidates for implantable and wearable electronics.[2] However, their widespread applications are heavily hindered by the sluggish kinetics of the cathodic oxygen reduction/evolution reaction (ORR/OER) during the discharging and charging process.[3] Noble metal-containing catalysts (i.e., Pt/C, IrO_2, RuO_2, and so forth.) are the state-of-the-art species toward these sluggish oxygen-involved reactions in air electrodes.[4] However, the scarcity and instability of noble metal-containing catalysts severely limit their large-scale applications, and the single functionality of ORR and OER is difficult to realize rechargeability.[5] Therefore, it is of great significance to construct inexpensive and highly active electrocatalysts possessing excellent stability and bifunctionality to substitute the aforementioned noble metal-based species.

Heteroatom-doped carbon materials are competitive candidates of ORR/OER bifunctional electrocatalysts because of their features of low cost, high chemical stability, tunable porous architecture, and controllable heteroatom active sites.[6] Doping with either electron-rich nitrogen/sulfur/phosphor atom[7−9] or electron-deficient boron/fluorine atoms[10,11] could convert electroneutral carbon into metal-free electrocatalyst by introducing abundant defects and large charge polarization, and these codoping atoms could further improve their OER/ORR reactivity.[12−14] In addition, multi-doped species could synergistically generate unique electronic properties and further enhance the electrocatalytic activities.[15] Over the last decade, mono-doped, dual-doped, and even tri-doped carbon electrocatalysts in various forms were engineered, and they exhibited superior electrocatalytic performance for ORR and OER.[16−19] To our best knowledge, previous studies usually focused on exploiting versatile heteroatom-abundant precursors and doping methods.[20] Despite momentous progress, the construction of innovative carbon nanomaterials for efficient multifunctional electrocatalysis is still challenging.[21] Most of the current studies focus on the design of precursors and doping strategies while ignoring the construction of heter-

Received: January 21, 2021
Accepted: March 2, 2021
Published: March 11, 2021

https://dx.doi.org/10.1021/acsami.1c01348
ACS Appl. Mater. Interfaces 2021, 13, 13328−13337

oatom-doped carbon with rationally designed nanostructures; however, these nanostructures might have crucial impact on their electrocatalytic performance.[22] As a unique three-dimensional (3D) morphology, the flower-shaped nanoarchitecture featuring special properties has demonstrated enhanced performance for electrocatalysis recently.[23−25] These unique open structures that consist of interconnected 2D nanosheets offer a large accessible surface area and more exposed functionalized sites, while the extended nanopetals interlace each other to ensure interfacial rapid ion diffusion and charge transport.[23] However, few methods have been reported to prepare carbon nanoflowers in terms of tedious procedures for synthesizing precursors.[25] Therefore, a controllable and efficient method to create functional carbon nanoflowers is highly desirable.

Covalent triazine frameworks (CTFs) are a class of promising polymer precursors for preparing heteroatom-doped carbons in terms of their intrinsic rich heteroatoms and abundant pore structures.[26−28] Compared with metal−organic frameworks (MOFs), the CTFs exhibited a higher thermal/chemical stability, providing a promising opportunity for the design of functional porous carbon materials. In recent years, different nanostructured heteroatom-doped carbons derived from CTFs (carbon nanospheres,[29−31] carbon nanotubes,[32] carbon nanosheets,[33] and so forth) have been rationally synthesized, and they exhibit a decent electrocatalytic activity for various electrochemical reaction.[34−36] 3D polymer nanoflowers possess high structural stability, which can significantly improve their carbonization yields.[37] Ultrasonic irradiation in the bulk solution gives rise to a new assembly mechanism for nanostructured polymers with various morphologies.[38−40] Therefore, the controllable synthesis of CTF-derived 3D heteroatom-doped porous carbon nanoflowers via ultrasonic synthesis is highly desired yet challenging.

Herein, we aim at introducing an ultrasound-triggered method for the construction of nitrogen, phosphorus, fluorine tri-doped porous carbons nanoflowers (NPF@CNFs). Triggered by ultrasound at room temperature, a piperazine-containing covalent triazine framework (P-CTF) was formed as the nanosheets and directly assembled into the shape of nanoflowers. Subsequent carbonization of P-CTF led to the in-situ formation of NPF@CNFs. The unique structural properties endowed the NPF@CNF-800 with outstanding bifunctional activities in the half-wave potential ($E_{1/2}$) of 0.85 V versus reversible hydrogen electrode (vs RHE) toward ORR and overpotential at 10 mA cm^{-2} (∼330 mV) toward OER, respectively, which significantly outperformed the commercial electrocatalysts. As a demonstration, both liquid-state and solid-state rechargeable Zn-air batteries using the NPF@CNF-800 as air electrodes delivered decent peak power density and excellent cycling stability.

2. EXPERIMENTAL METHODS

2.1. Synthesis of P-CTFs. The P-CTF nanoflower was prepared by ultrasound-induced polycondensation with the monomers of cyanuric chloride and piperazine, and meanwhile, triethylamine (TEA) solution was used as an acid-binding agent. Typically, 2.20 g of cyanuric chloride and 1.59 g of piperazine were dissolved in 200 mL of tetrahydrofuran (THF) to form a clear and uniform solution. After stirring for 2 min, 5.0 mL of TEA was added, and the above solution was kept under ultrasound conditions (200 W, 80 kHz) at room temperature for 4 h. After that, the resultant white precipitate denoted as P-CTF was filtered and washed with excess THF, acetone, ethanol, and water several times, and finally dried in vacuum at 80 °C overnight.

2.2. Synthesis of NPF@CNF-T. P-CTF (1.0 g) and 0.2 g of NH_4PF_6 salt were together placed in a corundum crucible and pyrolyzed at T °C (T = 700, 800, and 900) for 2 h in an Ar atmosphere at a flow rate of 50 mL min^{-1}, with a heating rate of 5 °C min^{-1} to obtain the NPF@CNF-Ts samples. After cooling to room temperature naturally, the as-obtained black powders were washed with water to remove the inactive and unstable components and then dried at 60 °C overnight. For comparison, 1.0 g of the P-CTF sample was also pyrolyzed by similar carbonization procedures, but without the NH_4PF_6 salt, which was named CNF-800.

3. RESULTS AND DISCUSSION

The preparation procedure of NPF@CNFs is illustrated in Scheme 1. Typically, the P-CTF nanoflowers assembled from nanosheets were synthesized via ultrasound-triggered polycondensation and assembly. Polycondensation was completed rapidly under ultrasound radiation, and the resulting CTF nanosheets were assembled into 3D nanoflowers in a short time. Subsequent carbonization of these P-CTF nanoflowers at the predesigned temperatures (700, 800, 900 °C) in the presence of NH_4PF_6 salt yielded uniform NPF@CNFs with abundant heteroatom active sites. The resultant products were denoted as NPF@CNF-700, NPF@CNF-800, NPF@CNF-900, respectively. A similar annealing procedure was conducted to fabricate P, F-free carbon nanoflowers (CNF-800).

Scheme 1. Procedures of Ultrasound-Triggered Assembly of P-CTF Nanoflowers for Synthesizing NPF@CNFs

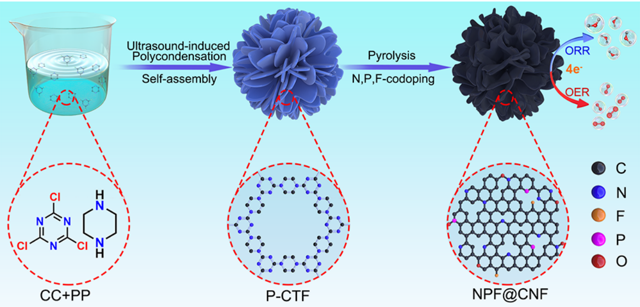

The P-CTF nanoflower was first characterized by the CP-MAS ^{13}C nuclear magnetic resonance (NMR) measurements. Figure S1 showed peaks at 43.8 and 163.3 ppm, which are assigned to the carbon signal in piperazine and triazine rings, respectively.[41,42] This result indicated the successful formation of P-CTF nanoflowers via condensation polymerization. The Fourier-transform infrared spectrum (FT-IR) of P-CTF (Figure S2) showed signals at 1520, 1440, and 1300 cm^{-1}, indicating the existence of triazine structures in the P-CTF framework.[43] In addition, the disappearance of the characteristic peak located at 850 cm^{-1} suggested the vanishing of C−Cl bonds, demonstrating that the P-CTF nanoflowers are integrated by covalent linking.[44] The X-ray diffraction (XRD) pattern demonstrated that the resulting P-CTF nanoflowers possessed certain ordered frameworks (Figure S3).[45] Thermogravimetric analysis (TGA) indicated that the P-CTF nanoflowers exhibited high thermal stability owing to the strong covalent-linked structures (Figure S4).[46] Meanwhile, the final weight of the P-CTF nanoflower remained as ∼25 wt % even up to 800 °C, confirming it is a promising polymer precursor for preparing functional heteroatom-doped nanocarbons. The thermal stability of the ultrasound-

https://dx.doi.org/10.1021/acsami.1c01348
ACS Appl. Mater. Interfaces 2021, 13, 13328−13337

synthesized CTF nanoflowers is much higher than the traditional synthetic method reported in our previous work,[47] indicating the great advantage of ultrasound synthesis. The nitrogen (N_2) adsorption/desorption and pore size distribution characteristics of the P-CTF nanoflower suggested that abundant micropores and mesopores were presented in the nanoflower framework (Figure S5).

Scanning electron microscopy (SEM) images of the P-CTF (Figure 1a, Figure S6a) presented a typical flower-like

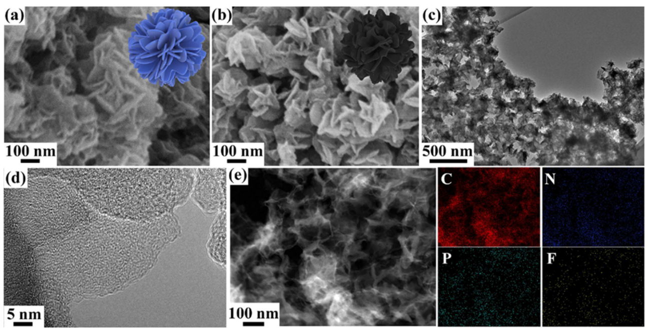

Figure 1. (a) SEM image of P-CTF nanoflowers, (b) SEM, (c) TEM, (d) HR-TEM images of NPF@CNF-800, and (e) STEM−EDS and elemental mappings of NPF@CNF-800 for C, N, P, and F elements.

morphology assembled from tightly connected nanosheets. This is due to the unique ultrasonic-assembly method, which is usually impossible using other traditional methods.[47] After pyrolysis, the flower-shaped morphology with fine nanopetals was well preserved (Figure 1b, Figure S6b), which is probably attributed to the stable reticular covalent texture in the P-CTF framework. The flower-like morphology could expose more active sites and form a well 3D conductive network, which was in favor of high-performance electrocatalytic activity.[23] Compared with the P-CTF precursor, the optimal NPF@CNF-800 showed a more rough surface owing to thermal shrinking caused by weight loss during carbonization.[48] Meanwhile, the morphology of NPF@CNF-800 was further evaluated using transmission electron microscopy (TEM) images, and a large number of lamellar architectures are presented in Figure 1c. The high-resolution TEM (HRTEM) image manifested that NPF@CNF-800 exhibited no obvious ordered carbon lattice fringes, suggesting that rich defects and amorphous structures existed. A large number of white dots are shown in Figure 1d to demonstrate the existence of micropores in the NPF@CNF-800.[47] The existence of these micropores facilitates the infiltration of the corresponding electrolyte, further enhancing the electrocatalytic activity.[49] Additionally, the N, P, and F atoms were homogeneously dispersed in the whole flower skeleton after pyrolysis, which was evidenced by energy-dispersive X-ray spectroscopy (EDS) mapping, as shown in Figure 1e. It could be demonstrated that the multiple heteroatom-embedded carbons with a nanoflower structure was successfully prepared. The pyrolytic temperature also exhibited an important effect on the electrocatalytic performance of as-obtained catalysts. At 700 °C, the flower-shaped structure was well maintained (Figure S7a,b), but the lower graphitization degree compared to NPF@CNF-800 resulted in poor conductivity (Table S1). However, the flower-like morphology was collapsed at a high temperature of 900 °C (Figure S7c,d), leading to a serious aggregation of the active sites. Hence, an appropriate pyrolysis temperature (800 °C) could not only preserve the well-defined flower-like morphology but also guarantee the electron/ion conduction and active center exposure during ORR and OER.[23]

The porous feature of the as-prepared NPF@CNFs was further measured via N_2 adsorption−desorption isotherms, as displayed in Figure 2a. All the P-CTF derived catalysts presented an obvious type-H_4 isotherm with a rapid increase of nitrogen absorption at both high and low pressure, demonstrating the coexistence of micropores and mesopores.[5] Applying these plots, the calculated Brunauer−Emmett−Teller (BET) specific surface area of NPF@CNF-800 was ~533.3 m^2 g^{-1}, which was higher than that of other NPF@CNFs (Table 1). Ascribing to the high specific surface area and hierarchical pore structure, favorable mass transfer could be

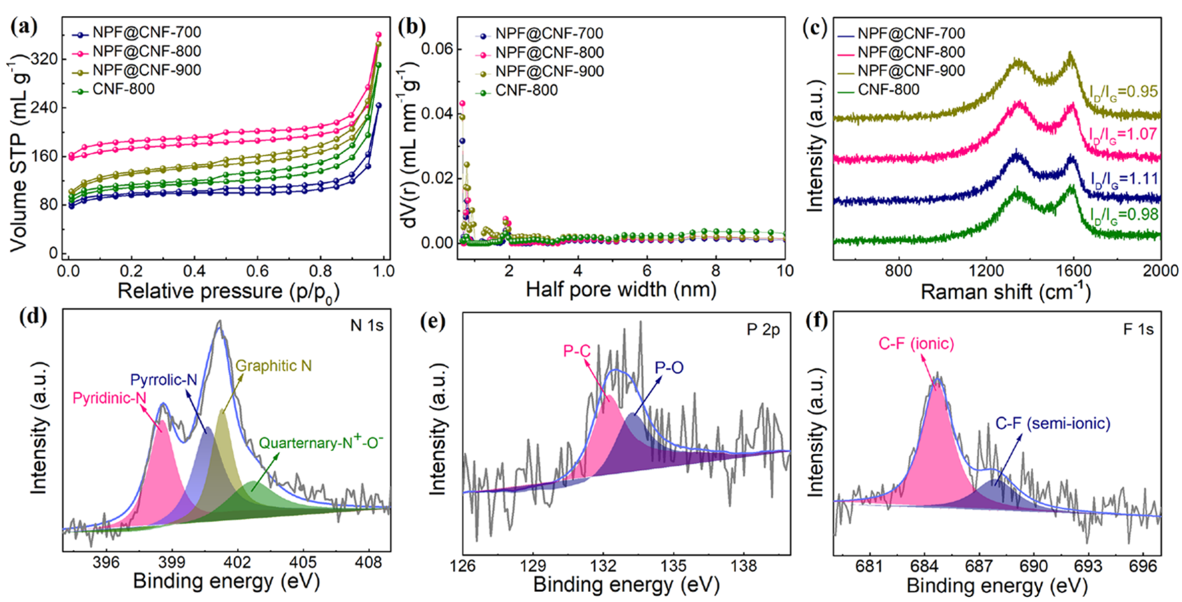

Figure 2. (a) Nitrogen adsorption/desorption isotherms, (b) pore size distributions of NPF@CNFs and CNF-800, (c) Raman spectra of NPF@CNFs and CNF-800, high-resolution (d) N 1 s, (e) P 2p, and (f) F 1 s XPS spectra of NPF@CNF-800.

https://dx.doi.org/10.1021/acsami.1c01348
ACS Appl. Mater. Interfaces 2021, 13, 13328−13337

Table 1. Summary of the BET Surface Area and Pore Volume for P-CTF, NPF@CNFs, and CNF-800 Samples

samples	BET surface area [m^2 g^{-1}]	micropore volume [mL g^{-1}]	mesopore volume [mL g^{-1}]	total pore volume [mL g^{-1}]
P-CTF	129.9	0.057	0.021	0.078
NPF@CNF-700	318.6	0.132	0.097	0.229
NPF@CNF-800	533.3	0.215	0.134	0.349
NPF@CNF-900	403.5	0.167	0.188	0.355
CNF-800	365.8	0.143	0.174	0.317

expected during the ORR/OER electrocatalytic process.[50] The pore size distribution (Figure 2b) also verified the existence of abundant micropores in NPF@CNF-800, which is in good consistency with the TEM results (Figure 1d). The hierarchical porosity exposed the heteroatom active surface and expedited the mass transport during the electrocatalytic process.[51]

The abundant hierarchical porous structures reflected relatively more defects in the NPF@CNFs.[52] Raman spectra in Figure 2c offer this helpful information, where the D (~1340 cm^{-1}) and G (~1580 cm^{-1}) bands belong to defects and ordered graphitic areas, respectively.[46] Multiple heteroatom-doped carbons can induce plentiful defects as ORR/OER electrocatalytic active centers, which was confirmed by the higher I_D/I_G value of the NPF@CNF-800 (~1.07) than that of the CNF-800 (~0.98). The I_D/I_G of the NPF@CNF-T reduced from 1.11 to 0.95 when the temperature increases from 700 to 900 °C. This suggested that the graphitization of the carbon backbone increased gradually, which was beneficial to improve the conductivity of the catalysts during the ORR/OER process.[33] Generally, the defects and conductivity synergistically contributed to the performance of the catalysts.[53] Therefore, the NPF@CNF-800 catalyst possessed suitable defect degrees and electric conductivity simultaneously, which were crucial for the ORR/OER electrocatalytic activity. Two characteristic broad peaks located at ~26 and 43° in the X-ray diffraction (XRD) patterns were consistent with the (002) and (010) planes of graphitic carbon that coexisted in the obtained electrocatalysts (Figure S8), further demonstrating the presence of abundant active defects.[54]

X-ray photoelectron spectroscopy (XPS) was further measured to obtain an insight into the corresponding chemical components of the nanoflower framework. The XPS survey spectra of all the obtained NPF@CNFs exhibited five peaks of C 1 s (284.9 eV), N 1 s (400.2 eV), P 2p (132.6 eV), F 1 s (686.5 eV), O 1 s (532.8 eV), which confirmed the successful formation of N, P, F tri-doped metal-free carbon catalysts (Figure S9). The doping contents of N, P, and F elements in the NPF@CNF-800 were 4.84, 1.38, and 0.64 at%, respectively (Table S2), matching well with the elemental analysis (Table S3). As depicted in Figure 2d, the core-level N 1 s XPS spectrum of NPF@CNF-800 was fitted to four peaks centered at ~398.4, 400.2, 401.1, and 403.1 eV, which were attributable to the pyridinic-N, pyrrolic-N, graphitic-N, and quarternary-N^+-O, respectively.[55] As shown in Figure S10, the pyridinic-N, graphitic N, and pyrrolic-N species were dominant, which were efficient electrocatalytic active sites for ORR.[20] The P 2p spectrum was divided into two distinguishable peaks located at ~132.2 and 133.6 eV, manifesting the existence of the P−C and P−O bonds, respectively (Figure 2e).[56] The introduction of P induced structural defects in the carbon framework and increased the electron delocalization due to the large radius of the P atom, which increased abundant electrocatalytic active sites and improved electrical conductivity.[57] Figure 2f exhibits typical ionic C−F bonds (684.9 eV) and semi-ionic (687. 8 eV) C−F bonds, both of which have been received as significant electrocatalytic active centers.[18] For comparison, the N, P, and F contents and the detailed doping types of NPF@CNF-700 and NPF@CNF-900 are displayed in Table S2 and Figures S11−12. It can be seen that the carbon content

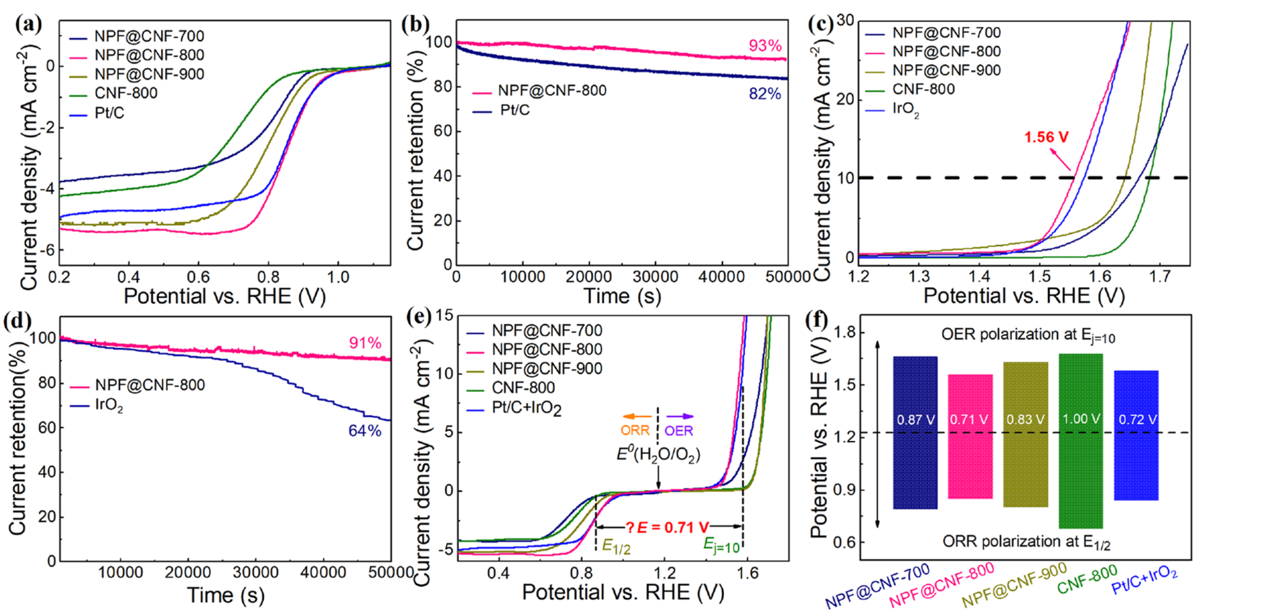

Figure 3. (a) LSV curves of NPF@CNFs, CNF-800, and Pt/C in O_2-saturated 0.1 M KOH. (b) Chronoamperometric responses of NPF@CNF-800 and Pt/C in O_2-saturated 0.1 M KOH. (c) OER polarization curves of NPF@CNFs, CNF-800, and IrO_2 in 1 M KOH at 5 mV s^{-1}. (d) Chronoamperometric responses of NPF@CNF-800 and IrO_2 catalysts in 1 M KOH. (e) LSV curves between the ORR and OER of NPF@CNFs, CNF-800, and Pt/C + IrO_2. (f) Potential differences between the OER current density at 10 mA cm^{-2} and the $E_{1/2}$ of ORR for NPF@CNFs, CNF-800, and Pt/C + IrO_2.

https://dx.doi.org/10.1021/acsami.1c01348
ACS Appl. Mater. Interfaces 2021, 13, 13328−13337

increased while the nitrogen, phosphorus, and fluorine contents decreased with the increasing carbonization temperature. N 1 s spectra showed that the species of nitrogen were different, and graphitic N became dominant with increasing pyrolysis temperature. The P 2p spectra of all the samples showed that the ratio of P−C and P−O was almost constant under a higher temperature. F 1 s spectra showed the ratio of semi-ionic C−F bonds increased while the ratio of ionic C−F bonds decreased when the pyrolysis temperature is increased. Heteroatom atoms were more likely to combine under higher calcination temperatures to form stable forms. The successful introduction of N, P, and F elements changed the surface charge distributions, and meanwhile, it increased the defects in the carbon matrix, both of which enhance the electrocatalytic performance.[58]

The ORR performance of the obtained catalysts was assessed by cyclic voltammetry (CV) testing in O_2- and N_2-saturated 0.1 M KOH electrolyte first. Figure S13 depicts the CV curves of NPF@CNF-800, displaying a characteristic rectangle without the redox peaks in the N_2-saturated electrolyte, while a distinct cathodic redox peak ∼0.81 V was observed in the O_2-saturated KOH electrolyte, affirming an obvious intrinsic ORR activity. In addition, the NPF@CNF-800 showed a more positive ORR peak potential than other obtained catalysts (Figure S14), suggesting the highest electrocatalytic activity for the ORR. This result clearly showed that multiple heteroatom doping and suitable pyrolysis temperatures could collectively improve the ORR activity of the resultant carbon nanoflowers. The linear sweep voltammetry (LSV) curves shown in Figure 3a demonstrated a more positive onset potential (E_{onset}) of 0.97 V vs. RHE and a half-wave potential ($E_{1/2}$) of 0.85 V vs RHE for NPF@CNF-800 than those of other as-obtained catalysts, which was also comparable to that of the Pt/C benchmark catalysts (E_{onset} = 1.01 V, $E_{1/2}$ = 0.86 V vs RHE). The ORR electrocatalytic performance of NPF-CNF-800 was significantly better than that of CNF-800, indicating that the multiple heteroatom doping remarkably increased the number of active sites. Additionally, the larger limited current density of NPF@CNF-800 demonstrated that it is more favorable for mass transfer and gas diffusion than other catalysts.[29] This result further confirmed that the excellent electrocatalytic activity of NPF@CNF-800 primarily originated from the rich exposed heteroatom active surface and hierarchical porosity. The electron-transfer number (N) of NPF@CNF-800 was calculated to be 3.85−3.97 by the Koutecky−Levich (K−L) plots, demonstrating a direct $4e^-$ reduction mechanism (Figure S15). Also, NPF@CNF-800 showed a higher double-layer capacitance (C_{dl}) (12.9 mF cm^{-2}) than other resultant catalysts, which was due to the relatively high specific surface area of NPF@CNF-800 (Figures S16−17). Meanwhile, a rotating ring-disk electrode (RRDE) was also conducted to further investigate the ORR mechanism. The low H_2O_2 yield (< 8.5%) indicated the almost complete O_2 reduction to H_2O, and N was obtained to be 3.84−3.95 at 0.3−0.8 V, implying that multiple heteroatom doping could enhance the selectivity for a desirable $4e^-$ approach (Figure S18). In addition, the J_K of NPF@CNF-800 (19.5 mA cm^{-2}) at 0.8 V was superior to that of Pt/C (18.2 mA·cm^{-2}), indicating that it had faster intrinsic kinetics (Figure S19). Additionally, the electrochemical impedance spectroscopy (EIS) measurements revealed that NPF@CNF-800 exhibited a significantly lower charge-transfer resistance compared with Pt/C and other CNFs catalysts (Figure S20), demonstrating a faster charge transfer process of the NPF@CNF-800 catalyst. No apparent decay (∼7%) was observed after 50, 000 s of continuous measurement (Figure 3b), while the Pt/C benchmark catalyst with a quick loss approaches 20%. Furthermore, a very small negative half-potential shift was observed after 10,000 CV cycles (Figure S21), further demonstrating the reliable stability of NPF@CNF-800 as an ORR electrocatalyst. Furthermore, almost no current changes were noticed for the NPF@CNF-800, whereas the commercial Pt/C catalyst showed an obvious decrease in current after adding 1 M methanol (Figure S22). It suggested that the NPF@CNF-800 also exhibited better tolerance to the methanol cross-over effect. Notably, the NPF@CNF-800 catalyst also manifested a half-wave potential of 0.73 V in 0.1 M $HClO_4$ (Figure S23), which further demonstrated that it exhibits a decent ORR activity in acid electrolytes.

To further study the structural and chemical stability of the NPF@CNF-800 catalyst, we characterized and discussed the morphology and composition of the as-prepared catalyst after the stability test. SEM and TEM observations revealed that the microstructure of NPF@CNF-800 was unchanged after the stability test (Figure S24), demonstrating that the as-prepared material exhibits good structural stability. Figure S25a shows the Raman spectra of the NPF@CNF-800 after the stability test. The ratio of the relative intensity between the D band and G band slightly increased to 1.10, which was mainly attributed to the slight corrosion of the carbon skeleton during the long testing process. The XRD pattern of the electrocatalyst after cycling still maintained the (002) and (010) peaks (Figure S25b), indicating that the nanoflower structures exhibit good chemical stability.

Remarkably, the resulting NPF@CNF catalysts also exhibited a high OER activity, which was evaluated by the LSV measurements in the 1 M KOH electrolyte. The overpotential of NPF@CNF-800 was ∼330 mV, which was superior to that of all the prepared catalysts and even commercial IrO_2 catalysts (Figure 3c and Figure S26), affirming the promotion of the OER activity by multiple heteroatom doping. Additionally, the OER performance of NPF@CNF-800 was also superior to most OER catalysts recently reported (Table S4). The result confirmed that the ultrasound method exhibits promising prospects in the preparation of defect-rich multiple heteroatom-doped electrocatalysts toward OER. In addition, a favorable OER kinetic process of the NPF@CNF-800 was confirmed by a relatively smaller Tafel slope than other catalysts (Figure S27). According to the i-t curves (Figure 3d), the NPF@CNF-800 retained more than 91% of its initial OER current density. However, the retention of the commercial IrO_2 catalyst was only ∼64% after the same test time, manifesting an excellent stability of NPF@CNF-800 for OER. Furthermore, the bifunctional activities of the NPF@CNFs were evaluated by the corresponding potential gap ΔE ($\Delta E = E_{j=10} - E_{1/2}$). The NPF@CNF-800 exhibited a low ΔE of 0.71 V (Figure 3e,f), which was lower than that of other catalysts and exceeded that of most reported metal-free electrocatalysts (Figure S28), affirming the outstanding bifunctional catalytic activity of NPF@CNF-800 toward both ORR and OER. To investigate the influence of the OER process on the ORR catalytic activity, the LSV curve of NPF@CNF-800 after the OER test is shown in Figure S29, in which the half-wave potential exhibited only a minimal negative shift of 13 mV.

https://dx.doi.org/10.1021/acsami.1c01348
ACS Appl. Mater. Interfaces 2021, 13, 13328−13337

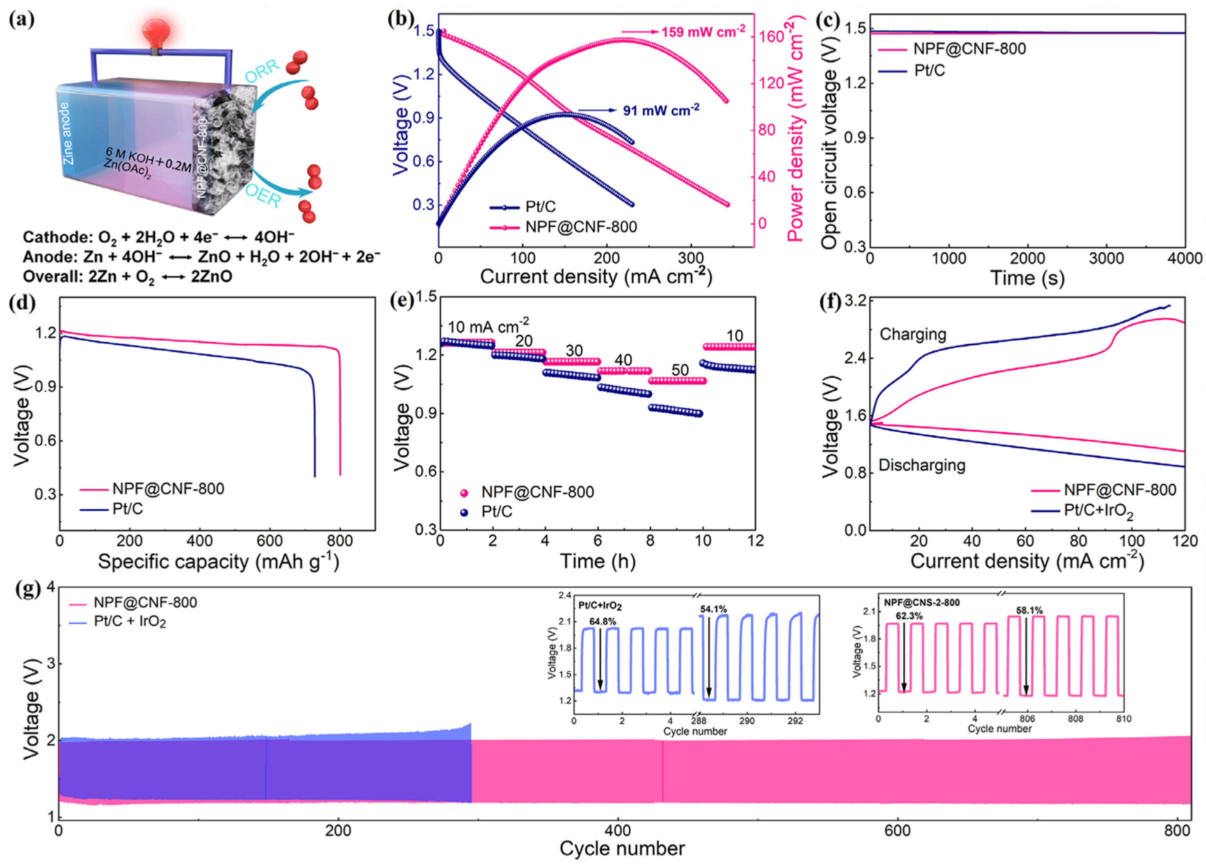

Figure 4. (a) Schematic illustration of the liquid Zn-air battery and its charge/discharge mechanism. (b) Discharge polarization curves and the power density curves of Zn-air batteries with NPF@CNF-800 and Pt/C cathodes, respectively. (c) OCV curves of the Zn-air batteries with NPF@CNF-800 and Pt/C cathodes, respectively. (d) Galvanostatic discharge curves of Zn-air batteries with the NPF@CNF-800 and Pt/C cathodes at 10 mA cm^{-2}. (e) Rate performance of the NPF@CNF-800 and Pt/C electrodes at a current density of 10, 20, 30, 40, 50, and 10 mA cm^{-2}, respectively. (f) Charge/discharge curves of rechargeable Zn-air batteries using the NPF@CNF-800 and Pt/C + IrO_2 cathodes. (g) Cycling performance of rechargeable Zn-air batteries with the NPF@CNF-800 and Pt/C + IrO_2 cathodes at 5 mA cm^{-2}. Insets in (g) showing the enlarged areas of the galvanostatic charge/discharge curves of NPF@CNF-800 and Pt/C + IrO_2, respectively.

Considering that NPF@CNF-800 could catalyze ORR and OER simultaneously, Zn−air batteries were fabricated using it as a cathode electrocatalyst (Figure 4a). Figure 4b shows the polarization profiles and the corresponding power density of the laboratory-made Zn-air batteries utilizing NPF@CNF-800 and the Pt/C electrocatalyst as the cathodes. The peak power density of NPF@CNF-800 was 159 mW cm^{-2}, which is 1.75 times that of the Pt/C catalyst (91 mW cm^{-2}). The good performance of the NPF@CNF-800 catalyst was attributed to its porous opened flower-shaped structure, which facilitated the rapid diffusion of oxygen and electrolyte to the active sites. Figure 4c illustrates that the NPF@CNF-800 delivered a more stable open-circuit voltage (OCV) than the Pt/C catalyst, suggesting that NPF@CNF-800 performed as a promising electrocatalyst under practical conditions. Moreover, the NPF@CNF-800-based battery also delivered a high specific capacity of 804 mAh g_{Zn}^{-1} at the current density of 10 mA cm^{-2}, which is superior to that of the commercial Pt/C catalyst (728 mAh g_{Zn}^{-1}). Meanwhile, the NPF@CNF-800 described a slight voltage loss and was more stable than the Pt/C + IrO_2-based battery, indicating excellent catalytic stability for ORR (Figure 4d). The Zn-air battery utilizing the NPF@CNF-800 electrode also exhibited a rate performance better than that of the commercial Pt/C cathode (Figure 4e). Although the Zn electrode was used up gradually in the continuous discharging process, the batteries could be recovered manually by replacing the new Zn plate and fresh KOH electrolyte for many cycles (Figure S30). The smaller voltage gap between the discharge and charge curves predicted that the NPF@CNF-800-based battery exhibits excellent rechargeability (Figure 4f).

The cycling stability of the Zn-air battery was tested to estimate the feasibility of NPF@CNF-800 in a practical environment. As demonstrated in Figure 4g and Figure S31, the Pt/C + IrO_2-based battery failed quickly with limited cyclability (48 h, 288 cycles), while the battery assembled using NPF@CNF-800 showed outstanding reversibility (135 h, 810 cycles). In the first cycle, the calculated energy efficiency of the Pt/C + IrO_2-based battery was 64.8%, which was higher than that of the NPF@CNF-800-based battery (62.3%). However, Pt/C and IrO_2 were both monofunctional catalysts with poor stability, and the corresponding energy efficiency observably decreased to 54.1% after merely 288 cycles. Whereas the NPF@CNF-800-based battery energy efficiency remained almost unchanged from 62.3% at the first cycle to 58.1% even after 810 cycles (inset of Figure 4g). The high specific surface areas of NPF@CNF-800 promoted sufficient electrochemical transfer on the electrocatalysts, which contributed to the stable cycling performance in the subsequent charging and discharging cycles.[59] Furthermore, the NPF@CNF-800-based electrode also showed excellent

https://dx.doi.org/10.1021/acsami.1c01348
ACS Appl. Mater. Interfaces 2021, 13, 13328−13337

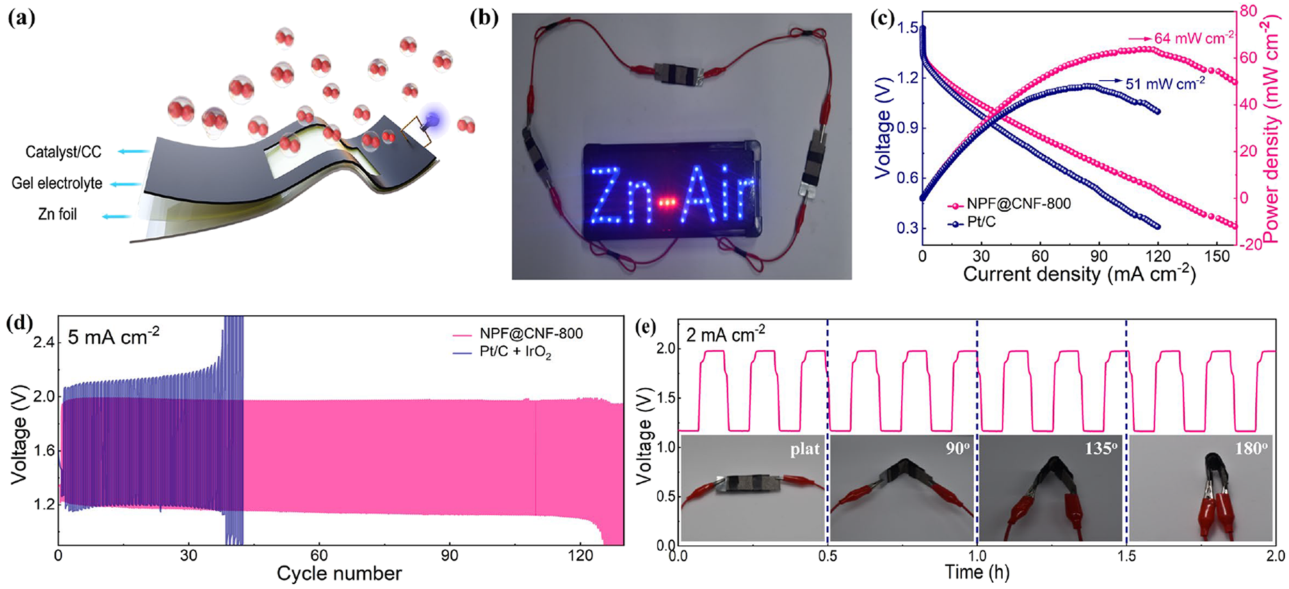

Figure 5. (a) Schematic representation of a solid-state rechargeable Zn-air battery with an NPF@CNF-800 cathode. (b) Photograph of LED bulbs powered using three solid-state rechargeable Zn-air batteries with the NPF@CNF-800 cathodes connected in series. (c) Polarization and power density curves of batteries with the NPF@CNF-800 and Pt/C cathodes. (d) Cycling performance of batteries with the NPF@CNF-800 and Pt/C cathodes at 5 mA cm^{-2}. (e) Galvanostatic discharge−charge curves of the battery with the NPF@CNF-800 cathodes at 2 mA cm^{-2} under different bending angles.

performance compared to some metal-based electrodes reported in the literature (Table S5). The high-power density and specific capacity, favorable rate performance, and excellent cycling performance unveil that the NPF@CNF-800 is a potential nonmetal bifunctional electrode for recyclable Zn-air batteries.

In recent years, the growing popularity of portable and wearable electronics has stimulated the rapid development of flexible batteries.[60] In this contribution, NPF@CNF-800 was fabricated into flexible solid-state Zn-air batteries employing polyvinyl alcohol hydrogel as a solid electrolyte (Figure 5a). As a further demonstration (Figure 5b), three batteries in series could lighten up a light-emitting diode (LED) viewing screen for a long time, showing its potential usage in flexible devices. Figure 5c exhibited that the NPF@CNF-800-based solid-state battery presented a better power density of 64 mW cm^{-2}, outperforming that of the Pt/C-based solid-state battery (51 mW cm^{-2}). Moreover, the discharge/charge cycle profiles of the NPF@CNF-800-based battery were more stable than those of the Pt/C + IrO_2-based battery (Figure 5d), indicating that it could work at a long-life operation with good stability. Furthermore, the performance of the NPF@CNF-800-based battery was comparable to that of other reported state-of-the-art heteroatom-doped carbon materials (Table S6). Figure S32 indicated that the NPF@CNF-800-based flexible Zn-air battery delivered an OCV of 1.33 V and good long-term stability. In addition, the OCV of the solid-state battery assembled with NPF@CNF-800 using a multimeter was 1.310 V, and it remained almost unchanged (1.309 V) at the bending state (Figure S33). Notably, the battery maintained constant charging (∼1.97 V) and discharging (∼1.18 V) that platformed at 2 mA cm^{-2} even after bending at 90°, 135°, and even at 180° (Figure 5e), verifying its practicability in electronics and wearable-electronics fields. Such superior performance was ascribed to the unique hierarchical nanoflower structures, plentiful heteroatom-doped active sites, and porous networks within the NPF@CNF-800.[61] Because the NPF@CNF-800 exhibits an excellent difunctional electrocatalytic performance, it might further replace the commercial noble-metal catalysts in the Zn-air battery industry.

4. CONCLUSIONS

In summary, we have introduced an ultrasound-triggered polycondensation and assembly strategy to synthesize a nanoflower-shaped CTF. Subsequent carbonization led to the in-situ formation of graphitized carbon nanoflowers with abundant distributions of N, P, and F heteroatom-doped active centers. As a result, the obtained NPF@CNF-800 electrocatalyst delivered both an impressive ORR ($E_{1/2}$ = 0.85 V vs RHE) and OER ($E_{j\,=\,10}$ = 1.56 V vs RHE) activity and remarkable cycling stability (retention above 90% after cycling for 50,000 s), outperforming those of most of the previously reported metal-free carbon electrocatalysts, and they are even superior to those of commercial Pt/Ir-based catalysts. Meanwhile, the liquid Zn-air batteries using NPF@CNF-800 as the cathode exhibited an excellent and stable OCV, significantly large peak power density, high specific capacity, and robust charge−discharge long-term stability (over 810 cycles). Furthermore, solid-state Zn-air batteries assembled with NPF@CNF-800 exhibited a peak power density of 64 mW cm^{-2}, decent cycling performance (more than 120 cycles), and reliable compatibility and performance even under extreme bending conditions. Our study paves a fresh avenue to designing high-efficiency metal-free electrocatalysts with a well-controllable microstructure for portable and wearable energy devices. On the one hand, it is helpful to solve the aggregation problem of catalytic active sites; on the other hand, this unique nanostructured carbon has a great potential to replace the state-of-the-art noble metal catalysts.

https://dx.doi.org/10.1021/acsami.1c01348
ACS Appl. Mater. Interfaces 2021, 13, 13328−13337

ASSOCIATED CONTENT

Supporting Information

The Supporting Information is available free of charge at https://pubs.acs.org/doi/10.1021/acsami.1c01348.

Materials, characterizations, electrochemical measurements, Zn-air battery measurements; solid-state ^{13}C NMR spectra, FT-IR spectra, XRD pattern, TGA curve, nitrogen adsorption/desorption isotherms of P-CTF; SEM images of P-CTF, NPF@CNFs; XRD pattern, XPS survey for NPF@CNF-800; CV curves, LSV curves, K-L plots and calculated electron-transfer numbers, ESCA, J_k and electrochemical impedance spectra of the resultant catalysts in O_2-saturated 0.1 M KOH; chronoamperometric responses of Pt/C and NPF@CNF-800; Tafel curves of OER catalysts; Zn-air battery performance of NPF@CNF-800; electrical conductivity of NPF@CNFs; elemental compositions of NPF@CNFs determined by XPS; comparison of carbon and nitrogen content of NPF@CNFs and CNF-800 by elemental analysis; comparison of NPF@CNF-800 with recently reported bifunctional ORR/OER catalysts under alkaline conditions; comparison of the performance of liquid-rechargeable Zn-air batteries with NPF@CNF-800 and other metal-doped carbon catalysts; and comparison of key parameters in flexible and solid-state rechargeable Zn-air batteries from the reported literature (PDF)

AUTHOR INFORMATION

Corresponding Authors

Kai A. I. Zhang − *Department of Materials Science, Fudan University, Shanghai 200433, P. R. China;* orcid.org/0000-0003-0816-5718; Email: kai_zhang@fudan.edu.cn

Chao Zhang − *State Key Laboratory for Modification of Chemical Fibers and Polymer Materials, College of Materials Science and Engineering, Innovation Center for Textile Science and Technology, Donghua University, Shanghai 201620, P. R. China;* orcid.org/0000-0003-1255-7183; Email: czhang@dhu.edu.cn

Authors

Yong Zheng − *State Key Laboratory for Modification of Chemical Fibers and Polymer Materials, College of Materials Science and Engineering, Innovation Center for Textile Science and Technology, Donghua University, Shanghai 201620, P. R. China*

Shan Chen − *State Key Laboratory for Modification of Chemical Fibers and Polymer Materials, College of Materials Science and Engineering, Innovation Center for Textile Science and Technology, Donghua University, Shanghai 201620, P. R. China*

Jixin Zhu − *Shaanxi Institute of Flexible Electronics (SIFE), Northwestern Polytechnical University (NPU), Xi'an 710072, P. R. China;* orcid.org/0000-0001-8749-8937

Jingsan Xu − *School of Chemistry, Physics and Mechanical Engineering, Queensland University of Technology, Brisbane, Queensland 4001, Australia;* orcid.org/0000-0003-1172-3864

Tianxi Liu − *State Key Laboratory for Modification of Chemical Fibers and Polymer Materials, College of Materials Science and Engineering, Innovation Center for Textile Science and Technology, Donghua University, Shanghai 201620, P. R. China; Key Laboratory of Synthetic and Biological Colloids, Ministry of Education, School of Chemical and Material Engineering, Jiangnan University, Wuxi 214122, P. R. China;* orcid.org/0000-0002-5592-7386

Complete contact information is available at: https://pubs.acs.org/10.1021/acsami.1c01348

Author Contributions

The manuscript was written through contributions of all authors. All authors have given approval to the final version of the manuscript.

Notes

The authors declare no competing financial interest.

ACKNOWLEDGMENTS

The authors are grateful for the financial support from the National Natural Science Foundation of China (51773035), the Shanghai Rising-Star Program (18QA1400200), and the Shanghai Scientific and Technological Innovation Project (18JC1410600).

REFERENCES

(1) Fu, J.; Cano, Z. P.; Park, M. G.; Yu, A.; Fowler, M.; Chen, Z. Electrically Rechargeable Zinc-Air Batteries: Progress, Challenges, and Perspectives. *Adv. Mater.* **2017**, *29*, No. 1604685.

(2) Chen, X.; Liu, B.; Zhong, C.; Liu, Z.; Liu, J.; Ma, L.; Deng, Y.; Han, X.; Wu, T.; Hu, W.; Lu, J. Ultrathin Co_3O_4 Layers with Large Contact Area on Carbon Fibers as High-Performance Electrode for Flexible Zinc-Air Battery Integrated with Flexible Display. *Adv. Energy Mater.* **2017**, *7*, No. 1700779.

(3) Meng, F.-L.; Liu, K.-H.; Zhang, Y.; Shi, M.-M.; Zhang, X.-B.; Yan, J.-M.; Jiang, Q. Recent Advances toward the Rational Design of Efficient Bifunctional Air Electrodes for Rechargeable Zn−Air Batteries. *Small* **2018**, *14*, No. 1703843.

(4) Tian, X.; Zhao, X.; Su, Y.-Q.; Wang, L.; Wang, H.; Dang, D.; Chi, B.; Liu, H.; Hensen, E. J. M.; Lou, X. W.; Xia, B. Y. Engineering Bunched Pt-Ni Alloy Nanocages for Efficient Oxygen Reduction in Practical Fuel Cells. *Science* **2019**, *366*, 850−856.

(5) Zhu, T.; Feng, Q.; Liu, S.; Zhang, C. Metallogel-Derived 3d Porous Carbon Nanosheet Composites as an Electrocatalyst for Oxygen Reduction Reaction. *Compos. Commun.* **2020**, *20*, No. 100376.

(6) Akula, S.; Sahu, A. K. Structurally Modulated Graphitic Carbon Nanofiber and Heteroatom (N,F) Engineering toward Metal-Free ORR Electrocatalysts for Polymer Electrolyte Membrane Fuel Cells. *ACS Appl. Mater. Interfaces* **2020**, *12*, 11438−11449.

(7) Yang, D.-S.; Bhattacharjya, D.; Inamdar, S.; Park, J.; Yu, J.-S. Phosphorus-Doped Ordered Mesoporous Carbons with Different Lengths as Efficient Metal-Free Electrocatalysts for Oxygen Reduction Reaction in Alkaline Media. *J. Am. Chem. Soc.* **2012**, *134*, 16127−16130.

(8) Nam, G.; Jang, H.; Sung, J.; Chae, S.; Soule, L.; Zhao, B.; Cho, J.; Liu, M. Evaluation of the Volumetric Activity of the Air Electrode in a Zinc-Air Battery Using a Nitrogen and Sulfur Co-Doped Metal-Free Electrocatalyst. *ACS Appl. Mater. Interfaces* **2020**, *12*, 57064−57070.

(9) Yang, Z.; Yao, Z.; Li, G.; Fang, G.; Nie, H.; Liu, Z.; Zhou, X.; Chen, X. A.; Huang, S. Sulfur-Doped Graphene as an Efficient Metal-Free Cathode Catalyst for Oxygen Reduction. *ACS Nano* **2012**, *6*, 205−211.

(10) Kong, X.; Huang, Y.; Liu, Q. Two-Dimensional Boron-Doped Graphyne Nanosheet: A New Metal-Free Catalyst for Oxygen Evolution Reaction. *Carbon* **2017**, *123*, 558−564.

(11) Lv, Y.; Yang, L.; Cao, D. Nitrogen and Fluorine-Codoped Porous Carbons as Efficient Metal-Free Electrocatalysts for Oxygen Reduction Reaction in Fuel Cells. *ACS Appl. Mater. Interfaces* **2017**, *9*, 32859−32867.

(12) Park, J. E.; Kim, M.-J.; Lim, M. S.; Kang, S. Y.; Kim, J. K.; Oh, S.-H.; Her, M.; Cho, Y.-H.; Sung, Y.-E. Graphitic Carbon Nitride-Carbon Nanofiber as Oxygen Catalyst in Anion-Exchange Membrane Water Electrolyzer and Rechargeable Metal-Air Cells. *Appl. Catal. B: Environ.* **2018**, *237*, 140−148.

(13) Zhu, X.; Hu, C.; Amal, R.; Dai, L.; Lu, X. Heteroatom-Doped Carbon Catalysts for Zinc-Air Batteries: Progress, Mechanism, and Opportunities. *Energy Environ. Sci.* **2020**, *13*, 4536−4563.

(14) Wang, J.; Kong, H.; Zhang, J.; Hao, Y.; Shao, Z.; Ciucci, F. Carbon-Based Electrocatalysts for Sustainable Energy Applications. *Prog. Mater. Sci.* **2021**, *116*, No. 100717.

(15) Zheng, Y.; Song, H.; Chen, S.; Yu, X.; Zhu, J.; Xu, J.; Zhang, K. A. I.; Zhang, C.; Liu, T. Metal-Free Multi-Heteroatom-Doped Carbon Bifunctional Electrocatalysts Derived from a Covalent Triazine Polymer. *Small* **2020**, *16*, No. 2004342.

(16) Zhao, Y.; Nakamura, R.; Kamiya, K.; Nakanishi, S.; Hashimoto, K. Nitrogen-Doped Carbon Nanomaterials as Non-Metal Electrocatalysts for Water Oxidation. *Nat. Commun.* **2013**, *4*, 2390.

(17) Wei, W.; Liang, H.; Parvez, K.; Zhuang, X.; Feng, X.; Müllen, K. Nitrogen-Doped Carbon Nanosheets with Size-Defined Mesopores as Highly Efficient Metal-Free Catalyst for the Oxygen Reduction Reaction. *Angew. Chem., Int. Ed.* **2014**, *53*, 1570−1574.

(18) Zhang, J.; Dai, L. Nitrogen, Phosphorus, and Fluorine Tri-Doped Graphene as a Multifunctional Catalyst for Self-Powered Electrochemical Water Splitting. *Angew. Chem., Int. Ed.* **2016**, *128*, 13490.

(19) Zhu, Y.-N.; Cao, C.-Y.; Jiang, W.-J.; Yang, S.-L.; Hu, J.-S.; Song, W.-G.; Wan, L.-J. Nitrogen, Phosphorus and Sulfur co-Doped Ultrathin Carbon Nanosheets as a Metal-Free Catalyst for Selective Oxidation of Aromatic Alkanes and the Oxygen Reduction Reaction. *J. Mater. Chem. A* **2016**, *4*, 18470−18477.

(20) Liu, X.; Dai, L. Carbon-Based Metal-Free Catalysts. *Nat. Rev. Mater.* **2016**, *1*, No. 16064.

(21) Hu, C.; Dai, L. Doping of Carbon Materials for Metal-Free Electrocatalysis. *Adv. Mater.* **2019**, *31*, No. 1804672.

(22) Tian, N.; Huang, H.; Du, X.; Dong, F.; Zhang, Y. Rational Nanostructure Design of Graphitic Carbon Nitride for Photocatalytic Applications. *J. Mater. Chem. A* **2019**, *7*, 11584−11612.

(23) Chen, S.; Koshy, D. M.; Tsao, Y.; Pfattner, R.; Yan, X.; Feng, D.; Bao, Z. Highly Tunable and Facile Synthesis of Uniform Carbon Flower Particles. *J. Am. Chem. Soc.* **2018**, *140*, 10297−10304.

(24) Hwang, J.; Walczak, R.; Oschatz, M.; Tarakina, N. V.; Schmidt, B. V. K. J. Micro-Blooming: Hierarchically Porous Nitrogen-Doped Carbon Flowers Derived from Metal-Organic Mesocrystals. *Small* **2019**, *15*, No. 1901986.

(25) Xu, Z.; Zhuang, X.; Yang, C.; Cao, J.; Yao, Z.; Tang, Y.; Jiang, J.; Wu, D.; Feng, X. Nitrogen-Doped Porous Carbon Superstructures Derived from Hierarchical Assembly of Polyimide Nanosheets. *Adv. Mater.* **2016**, *28*, 1981−1987.

(26) Kuhn, P.; Antonietti, M.; Thomas, A. Porous, Covalent Triazine-Based Frameworks Prepared by Ionothermal Synthesis. *Angew. Chem., Int. Ed.* **2008**, *47*, 3450−3453.

(27) Krishnaraj, C.; Jena, H. S.; Leus, K.; Van Der Voort, P. Covalent Triazine Frameworks − a Sustainable Perspective. *Green Chem.* **2020**, *22*, 1038.

(28) Ren, S.; Bojdys, M. J.; Dawson, R.; Laybourn, A.; Khimyak, Y. Z.; Adams, D. J.; Cooper, A. I. Porous, Fluorescent, Covalent Triazine-Based Frameworks Via Room-Temperature and Microwave-Assisted Synthesis. *Adv. Mater.* **2012**, *24*, 2357−2361.

(29) Zhu, Y.; Chen, X.; Liu, J.; Zhang, J.; Xu, D.; Peng, W.; Li, Y.; Zhang, G.; Zhang, F.; Fan, X. Rational Design of Fe/N/S-Doped Nanoporous Carbon Catalysts from Covalent Triazine Frameworks for Efficient Oxygen Reduction. *ChemSusChem* **2018**, *11*, 2402−2409.

(30) Wang, D.-G.; Wang, H.; Lin, Y.; Yu, G.; Song, M.; Zhong, W.; Kuang, G.-C. Synthesis and Morphology Evolution of Ultrahigh Content Nitrogen-Doped, Micropore-Dominated Carbon Materials as High-Performance Supercapacitors. *ChemSusChem* **2018**, *11*, 3932−3940.

(31) Zhu, J.; Yang, J.; Xu, Z.; Wang, J.; Nuli, Y.; Zhuang, X.; Feng, X. Silicon Anodes Protected by a Nitrogen-Doped Porous Carbon Shell for High-Performance Lithium-Ion Batteries. *Nanoscale* **2017**, *9*, 8871−8878.

(32) He, Y.; Gehrig, D.; Zhang, F.; Lu, C.; Zhang, C.; Cai, M.; Wang, Y.; Laquai, F.; Zhuang, X.; Feng, X. Highly Efficient Electrocatalysts for Oxygen Reduction Reaction Based on 1d Ternary Doped Porous Carbons Derived from Carbon Nanotube Directed Conjugated Microporous Polymers. *Adv. Funct. Mater.* **2016**, *26*, 8255−8265.

(33) Jiao, L.; Hu, Y.; Ju, H.; Wang, C.; Gao, M.-R.; Yang, Q.; Zhu, J.; Yu, S.-H.; Jiang, H.-L. From Covalent Triazine-Based Frameworks to N-Doped Porous Carbon/Reduced Graphene Oxide Nanosheets: Efficient Electrocatalysts for Oxygen Reduction. *J. Mater. Chem. A* **2017**, *5*, 23170−23178.

(34) Gao, Y.; Zhi, C.; Cui, P.; Zhang, K. A. I.; Lv, L.-P.; Wang, Y. Halogen-Functionalized Triazine-Based Organic Frameworks Towards High Performance Supercapacitors. *Chem. Eng. J.* **2020**, *400*, No. 125967.

(35) Vadiyar, M. M.; Liu, X.; Ye, Z. Macromolecular Polyethynylbenzonitrile Precursor-Based Porous Covalent Triazine Frameworks for Superior High-Rate High-Energy Supercapacitors. *ACS Appl. Mater. Interfaces* **2019**, *11*, 45805−45817.

(36) Li, Z.; Huang, D.; Zhou, C.; Xue, W.; Lei, L.; Deng, R.; Yang, Y.; Chen, S.; Wang, W.; Wang, Z. Metal-Free Carbon Nitride with Boosting Photo-Redox Ability Realized by the Controlled Carbon Dopants. *Chem. Eng. J.* **2020**, *382*, No. 122657.

(37) Huang, J.; Chen, Y.; Leng, K.; Liu, S.; Chen, Z.; Chen, L.; Wu, D.; Fu, R. Morphology-Persistent Carbonization of Self-Assembled Block Copolymers for Multifunctional Coupled Two-Dimensional Porous Carbon Hybrids. *Chem. Mater.* **2020**, *32*, 8971−8980.

(38) Wei, X.; Zhang, G.; Zhou, L.; Li, J. Synthesis and Characterization of Hydrophobic Amino-Based Polyphosphazene Microspheres with Different Morphologies Via Two Strategies. *Appl. Surf. Sci.* **2017**, *419*, 744−752.

(39) Hujjatul Islam, M.; Paul, M. T. Y.; Burheim, O. S.; Pollet, B. G. Recent Developments in the Sonoelectrochemical Synthesis of Nanomaterials. *Ultrason. Sonochem.* **2019**, *59*, No. 104711.

(40) Zhu, X.; Xia, Y.; Zhang, X.; Al-Khalaf, A. A.; Zhao, T.; Xu, J.; Peng, L.; Hozzein, W. N.; Li, W.; Zhao, D. Synthesis of Carbon Nanotubes@Mesoporous Carbon Core−Shell Structured Electrocatalysts Via a Molecule-Mediated Interfacial Co-Assembly Strategy. *J. Mater. Chem. A* **2019**, *7*, 8975−8983.

(41) Guo, S.; Yang, P.; Zhao, Y.; Yu, X.; Wu, Y.; Zhang, H.; Yu, B.; Han, B.; George, M. W.; Liu, Z. Direct Z-Scheme Heterojunction of SnS_2/Sulfur-Bridged Covalent Triazine Frameworks for Visible-Light-Driven CO_2 Photoreduction. *ChemSusChem* **2020**, *13*, 6278−6283.

(42) Cui, Y.; Ding, Z.; Fu, X.; Wang, X. Construction of Conjugated Carbon Nitride Nanoarchitectures in Solution at Low Temperatures for Photoredox Catalysis. *Angew. Chem., Int. Ed.* **2012**, *51*, 11814−11818.

(43) Wang, K.; Yang, L.-M.; Wang, X.; Guo, L.; Cheng, G.; Zhang, C.; Jin, S.; Tan, B.; Cooper, A. Covalent Triazine Frameworks Via a Low-Temperature Polycondensation Approach. *Angew. Chem., Int. Ed.* **2017**, *56*, 14149−14153.

(44) Jones, D. C.; Carr, C. M.; Cooke, W. D.; Lewis, D. M. Investigating the Photo-Oxidation of Wool Using Ft-Raman and Ft-Ir Spectroscopies. *Text. Res. J.* **2016**, *68*, 739−748.

(45) Zhao, H.; Jin, Z.; Su, H.; Jing, X.; Sun, F.; Zhu, G. Targeted Synthesis of a 2D Ordered Porous Organic Framework for Drug Release. *Chem. Commun.* **2011**, *47*, 6389−6391.

(46) Zheng, Y.; Chen, S.; Song, H.; Guo, H.; Zhang, K. A. I.; Zhang, C.; Liu, T. Nitrogen-Doped Hollow Carbon Nanoflowers from a Preformed Covalent Triazine Framework for Metal-Free Bifunctional Electrocatalysis. *Nanoscale* **2020**, *12*, 14441−14447.

(47) Chen, S.; Zheng, Y.; Zhang, B.; Feng, Y.; Zhu, J.; Xu, J.; Zhang, C.; Feng, W.; Liu, T. Cobalt, Nitrogen-Doped Porous Carbon Nanosheet-Assembled Flowers from Metal-Coordinated Covalent

https://dx.doi.org/10.1021/acsami.1c01348
ACS Appl. Mater. Interfaces 2021, 13, 13328−13337

Organic Polymers for Efficient Oxygen Reduction. *ACS Appl. Mater. Interfaces* **2019**, *11*, 1384−1393.

(48) Lu, X. F.; Chen, Y.; Wang, S.; Gao, S.; Lou, X. W. Interfacing Manganese Oxide and Cobalt in Porous Graphitic Carbon Polyhedrons Boosts Oxygen Electrocatalysis for Zn-Air Batteries. *Adv. Mater.* **2019**, *31*, No. 1902339.

(49) Tong, Z.; Yang, D.; Zhao, X.; Shi, J.; Ding, F.; Zou, X.; Jiang, Z. Bio-Inspired Synthesis of Three-Dimensional Porous G-C_3N_4@ Carbon Microflowers with Enhanced Oxygen Evolution Reactivity. *Chem. Eng. J.* **2018**, *337*, 312−321.

(50) Li, L.; Zhang, Y.; Lu, H.; Wang, Y.; Xu, J.; Zhu, J.; Zhang, C.; Liu, T. Cryopolymerization Enables Anisotropic Polyaniline Hybrid Hydrogels with Superelasticity and Highly Deformation-Tolerant Electrochemical Energy Storage. *Nat. Commun.* **2020**, *11*, 62−72.

(51) Lu, X. F.; Zhang, S. L.; Shangguan, E.; Zhang, P.; Gao, S.; Lou, X. W. Nitrogen-Doped Cobalt Pyrite Yolk-Shell Hollow Spheres for Long-Life Rechargeable Zn-Air Batteries. *Adv. Sci.* **2020**, *7*, No. 2001178.

(52) Douka, A. I.; Xu, Y.; Yang, H.; Zaman, S.; Yan, Y.; Liu, H.; Salam, M. A.; Xia, B. Y. A Zeolitic-Imidazole Frameworks-Derived Interconnected Macroporous Carbon Matrix for Efficient Oxygen Electrocatalysis in Rechargeable Zinc-Air Batteries. *Adv. Mater.* **2020**, *32*, No. 2002170.

(53) Rao, P.; Cui, P.; Wei, Z.; Wang, M.; Ma, J.; Wang, Y.; Zhao, X. Integrated N-Co/Carbon Nanofiber Cathode for Highly Efficient Zinc-Air Batteries. *ACS Appl. Mater. Interfaces* **2019**, *11*, 29708−29717.

(54) Lin, X.; Peng, P.; Guo, J.; Xiang, Z. Reaction Milling for Scalable Synthesis of N, P-Codoped Covalent Organic Polymers for Metal-Free Bifunctional Electrocatalysts. *Chem. Eng. J.* **2019**, *358*, 427.

(55) Guo, H.; Feng, Q.; Zhu, J.; Xu, J.; Li, Q.; Liu, S.; Xu, K.; Zhang, C.; Liu, T. Cobalt Nanoparticle-Embedded Nitrogen-Doped Carbon/Carbon Nanotube Frameworks Derived from a Metal-Organic Framework for Tri-Functional ORR, OER and HER Electrocatalysis. *J. Mater. Chem. A* **2019**, *7*, 3664−3672.

(56) Wang, M.; Li, Y.; Fang, J.; Villa, C. J.; Xu, Y.; Hao, S.; Li, J.; Liu, Y.; Wolverton, C.; Chen, X.; Dravid, V. P.; Lai, Y. Superior Oxygen Reduction Reaction on Phosphorus-Doped Carbon Dot/Graphene Aerogel for All-Solid-State Flexible Al-Air Batteries. *Adv. Energy Mater.* **2020**, *10*, No. 1902736.

(57) Lei, W.; Deng, Y.-P.; Li, G.; Cano, Z. P.; Wang, X.; Luo, D.; Liu, Y.; Wang, D.; Chen, Z. Two-Dimensional Phosphorus-Doped Carbon Nanosheets with Tunable Porosity for Oxygen Reactions in Zinc-Air Batteries. *ACS Catal.* **2018**, *8*, 2464−2472.

(58) Wang, L.; Wang, Y.; Wu, M.; Wei, Z.; Cui, C.; Mao, M.; Zhang, J.; Han, X.; Liu, Q.; Ma, J. Nitrogen, Fluorine, and Boron Ternary Doped Carbon Fibers as Cathode Electrocatalysts for Zinc-Air Batteries. *Small* **2018**, *14*, No. 1800737.

(59) Guo, Y.; Yao, S.; Gao, L.; Chen, A.; Jiao, M.; Cui, H.; Zhou, Z. Boosting Bifunctional Electrocatalytic Activity in S and N Co-Doped Carbon Nanosheets for High-Efficiency Zn-Air Batteries. *J. Mater. Chem. A* **2020**, *8*, 4386−4395.

(60) Li, M.; Liu, B.; Fan, X.; Liu, X.; Liu, J.; Ding, J.; Han, X.; Deng, Y.; Hu, W.; Zhong, C. Long-Shelf-Life Polymer Electrolyte Based on Tetraethylammonium Hydroxide for Flexible Zinc-Air Batteries. *ACS Appl. Mater. Interfaces* **2019**, *11*, 28909−28917.

(61) Li, X.; Guan, B. Y.; Gao, S.; Lou, X. W. (. D.). A General Dual-Templating Approach to Biomass-Derived Hierarchically Porous Heteroatom-Doped Carbon Materials for Enhanced Electrocatalytic Oxygen Reduction. *Energy Environ. Sci.* **2019**, *12*, 648−655.

https://dx.doi.org/10.1021/acsami.1c01348
ACS Appl. Mater. Interfaces 2021, 13, 13328−13337